Biomimetic Intelligence and Robotics 4 (2024) 100176

Contents lists available at ScienceDirect

Biomimetic Intelligence and Robotics

journal homepage: www.elsevier.com/locate/birob

Research Article

A bionic robotic ankle driven by the multiple pneumatic muscle actuators

Delei Fang *, Fangyuan Ren, Jianwei Wang, Pan Li, Lin Cao *, Junxia Zhang

Tianjin Key Laboratory of Integrated Design and On-line Monitoring for Light Industry & Food Machinery and Equipment, College of Mechanical Engineering, Tianjin University of Science and Technology, Tianjin 300222, China

ARTICLE INFO

Article history:
Received 4 June 2024
Revised 26 July 2024
Accepted 1 August 2024
Available online 12 August 2024

Keywords:
Pneumatic muscle actuator
Bionic robotic ankle
Load matching
Recruiting strategy

ABSTRACT

The traditional pneumatic muscle robot joint has weak load capacity and low control precision. This paper proposes a bionic robotic ankle driven by multiple pneumatic muscle actuators. The structural design of the bionic robotic ankle and the drive mechanism that imitates human muscle recruitment are introduced. A dynamic model of the ankle and a static model of the pneumatic muscle actuator are established to analyze the driving characteristics. The multi-muscle recruiting strategy and load matching control method are optimized, and the output characteristics are simulated, including the robotic ankle driven by a single pneumatic muscle actuator, the robotic ankle driven by dual pneumatic muscle actuators, and the bionic ankle driven by multiple pneumatic muscle actuators. A prototype and testing platform are developed, and experimental research is carried out to validate the theoretical analysis and simulation. The results show that the bionic robotic ankle driven by multiple pneumatic muscle actuators can match varied loads, effectively reducing angle error and increasing output force.

1. Introduction

Soft actuators have higher flexibility than rigid actuators, making them highly promising for industrial production, medical rehabilitation, and military equipment [1–3]. Among soft actuators, the pneumatic muscle actuator (PMA) has been widely studied. Its structure, consisting of woven non-stretchable fibers and elastic inner capsules, is easy to manufacture, low-cost, and flexible. Driven by compressed gas, it has high power density and safety, making it particularly suitable for robotic joints [4–6].

Currently, there are three main types of robotic joints driven by PMAs: the unilateral PMA, the PMA with a spring, and the bilateral PMA [7,8]. Extensive research has been conducted on these designs. Zhong uses a single PMA to drive a robotic joint that mimics a frog's leg, enabling a bionic foot to jump [9]. Tsai develops a novel 2-DOF lower limb rehabilitation robot using springs and a single PMA [10,11]. Jamil uses springs and a PMA to drive a robotic joint capable of resisting external interference to achieve different motion modes [12]. Iijima constructs a bionic flexible joint suitable for one-legged jumping robots based on the antagonistic arrangement of the McKibben PMA [13]. Liang proposes an energy-based nonlinear control method to achieve accurate positioning control using an antagonistic arrangement of a joint with springs and PMAs [14]. Zhao realizes wrist motion using an antagonistic PMA arrangement and proposes an adaptive collaborative control strategy based on real-time joint impedance estimation [15]. Chu develops a 4-DOF robotic arm with wearable features for upper limb rehabilitation, utilizing a combination of spring-PMA and bilateral PMAs [16]. Xie presents a compact elbow exoskeleton based on PMA, employing a novel winding and bionic attachment method to anchor the PMA, achieving high output torque [17]. Khan develops a PMA-based stroke rehabilitation device for aiding elbow and knee flexion and extension [18]. Wang designs a novel soft parallel robot dedicated to automated wrist rehabilitation, utilizing a modified 6-SPS/PS parallel mechanism structure to drive the patient's wrist joint through various movements [19].

In addition to structural design, scholars have also researched driving control technology. Nguyen develops an adaptive fast terminal sliding mode controller for a robotic arm with PMA, employing fuzzy logic techniques to approximate nonlinear functions and a PID controller as a compensator with online learning capability [20]. Chen proposes a 4-DOF upper limb robotic exoskeleton for supporting shoulder and elbow movements, actuated by a PAM via a cable, primarily for passive rehabilitation [21]. Chi designs a rehabilitation robotic device driven by two antagonistic pairs of PAMs for stroke patients, using a knowledge-guided data-driven modeling approach to propose an adaptive feed-forward-feedback control method [22]. Tsai develops a 1-DOF robotic lower limb system driven by a novel single PAM with a torsion spring, utilizing a fuzzy sliding mode controller (FSMC) for path tracking [23]. Chu designs a wearable upper-limb

* Corresponding authors.
E-mail addresses: fangdelei@tust.edu.cn (D. Fang), caolin@tust.edu.cn (L. Cao).

https://doi.org/10.1016/j.birob.2024.100176

power-assist exoskeleton system (UPES) [24]. Liu proposes a new coordinated path planning and impedance control method for a modular exoskeleton elbow and wrist rehabilitation robot driven by PAM [25].

Existing research shows that the unilateral PMA joint has a simple structure but suffers from larger vibrations and limited motion range due to the reverse motion of its own weight. The spring and PMA joint need to overcome the spring force, causing a cushioning effect and reducing driving capacity. The bilateral PMA joint can achieve bidirectional rotation, with PMAs on both sides working as agonistic and antagonistic muscles, providing a wide range of movement and flexibility, which is favored by researchers [26]. However, most bilateral PMA joints are driven by a single PMA on one side, resulting in insufficient output force for large loads. To increase carrying capacity, researchers have gradually equipped multiple bionic Muscle Actuators. The Clone Hand consists of 37 McKibben muscles with 24 degrees of freedom. These muscles have efficient contractile performance, provide powerful driving force [27]. Hoang et al. developed Roboy 3.0, a robot that imitates the workings and morphology of the human musculoskeletal system. This design allows energy to be stored in the muscles, giving the robot flexibility [28]. Nevertheless, the existing motion control focuses on algorithms to improve accuracy, ignoring the influence of different PMA selections on motion, which often lacks load matching, leading to large angle errors. Yang et al. have developed a bionic robotic joint that accurately replicates the musculoskeletal structure of humans. This novel design incorporates the mechanical intelligence of the biological joint, significantly improving the flexibility and load capacity of the robotic joint [29].

The above literature shows that the bionic structure is important for the bionic robotic joints, and the load matching control method is also critical for motion performance. The paper proposes a bionic robotic ankle driven by multiple pneumatic muscle actuators (a Multi-PMA bionic robotic ankle) based on a driving mechanism. The research and design focus on the bionic structure, force matching strategy, and position-based control approach. The paper's main contributions are twofold: (1) In the structural design, multiple pneumatic muscle actuators are symmetrically arranged to function as agonistic and antagonistic muscles, improving load capacity and position accuracy. (2) In terms of the driving mechanism, the driving units recruit PMAs in real-time based on the load to achieve load matching control, enhancing the robotic ankle's motion performance.

The article is arranged as follows. The second part introduces the driving mechanism of the bionic multi-muscle unit and the concept of structural design. In the third part, the dynamic model of the ankle and the static model of the PMA are established to analyze the driving characteristics. The fourth part covers the control simulation, where the output angle and output force are simulated based on the multi-muscle unit recruiting strategy. The fifth part discusses the experiment, including the development of the prototype and testing platform to analyze the motion characteristics of different types of ankles.

2. Design and analysis

2.1. Driving mechanism

The power of the human joint comes from muscles, which obtain energy from blood and signals from nerves to drive the joint to move smoothly, as shown in Fig. 1. The smallest working unit in the muscle, called the motor unit, includes the motor neuron and the muscle fiber. Due to the varying loads on the joint, motor units are usually selectively activated when muscles drive the joint to move. To ensure that the output force matches the load, the joint and muscle have evolved the following features: (a) skeletal muscle contains multiple motor units, and (b) skeletal muscle recruits different motor units to drive joints under different loads.

The multi-PMA bionic robotic ankle proposed in this paper mimics the skeletal-muscle structure of the human ankle, as shown in Fig. 1. Pneumatic muscle actuators are arranged on both sides of the ankle. The gas pipe mimics human blood vessels to provide energy, and gas valves control the gas flow and pressure into the PMAs. Control signals act like human nerve signals, including pulse signals that control the action of valves and sensor signals that detect ankle motion. To enable the bionic robotic ankle to drive variable loads smoothly, the driving mechanism of the multi-PMA imitates the driving mechanism of human skeletal muscle: the rotation of the ankle is driven by multi-PMA on both sides, which act as agonistic and antagonistic muscles. Additionally, the agonistic and antagonistic muscles will recruit different numbers of PMAs to achieve load-matching control with high flexibility and energy efficiency.

2.2. Dynamic model

The bionic robotic ankle performs plantar and dorsiflexion movements, which are simplified into a two-link structure, as shown in Fig. 2. The dynamic model of the bionic robotic ankle is established using the Lagrange equation. It is assumed that the center of mass is located at the midpoint of the rod and that the load is applied precisely at the endpoint.

According to the ankle coordinate system, the center of mass m_1 of rod 1 can be determined.

$$\begin{cases} x_1 = \frac{1}{2} d_1 \sin\theta_1 \\ y_1 = -d_0 - \frac{1}{2} d_1 \cos\theta_1 \end{cases} \tag{1}$$

where d_0 is the length of the calf, d_1 is the length from the shaft to the sole, and θ_1 is the angle of rotation.

Similarly, the position of the load centroid m_2 can be determined.

$$\begin{cases} y_2 = -d_0 - d_1 \cos\theta_1 \\ x_2 = d_1 \sin\theta_1 \end{cases} \tag{2}$$

The derivative of Eq. (1) yields the velocity of the center of mass m_1 of rod 1.

$$\begin{cases} \dot{x}_1 = \frac{1}{2} d_1 \cos\theta_1 \dot{\theta}_1 \\ \dot{y}_1 = \frac{1}{2} d_1 \sin\theta_1 \dot{\theta}_1 \end{cases} \tag{3}$$

By differentiating Eq. (2), the velocity of the load centroid m_2 is obtained.

$$\begin{cases} \dot{x}_2 = d_1 \cos\theta_1 \dot{\theta}_1 \\ \dot{y}_2 = d_1 \sin\theta_1 \dot{\theta}_1 \end{cases} \tag{4}$$

The total kinetic energy is denoted by K.

$$K = \frac{1}{2} J_1 \dot{\theta}_1^2 + \frac{1}{2} m_1 v_1^2 + \frac{1}{2} m_2 v_2^2 \tag{5}$$

where J_1 is the moment of inertia of rod 1. m_0, m_1, m_2 represent the masses of rod 0, rod 1 and the load, respectively. $v_1 = \sqrt{\dot{x}_1^2 + \dot{y}_1^2}$, $v_2 = \sqrt{\dot{x}_2^2 + \dot{y}_2^2}$.

The total potential energy is denoted by P.

$$P = -m_1 g \left(d_0 + \frac{1}{2} d_1 \cos\theta_1 \right) - m_2 g \left(d_0 + d_1 \cos\theta_1 \right) \tag{6}$$

The kinetic equation can be established.

$$L = K - P \tag{7}$$

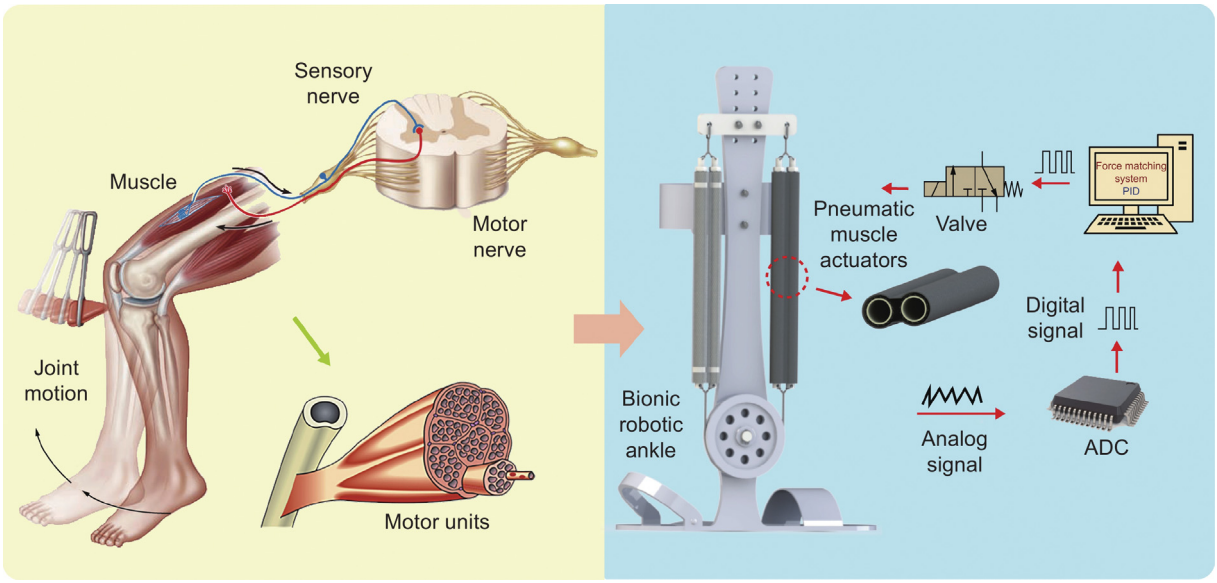

Fig. 1. Design of bionic robotic ankle imitating human multi-muscle structure.

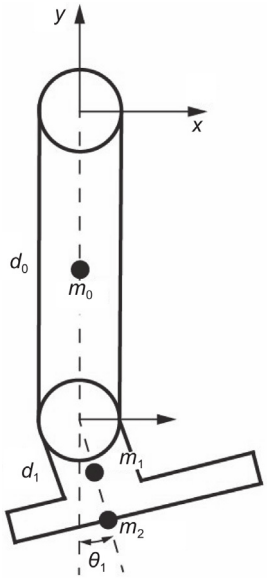

Fig. 2. Diagram of simplified structure of the ankle.

where L is the Lagrange function. The expression for the expected torque is obtained as follows.

$$T_i = \frac{\partial}{\partial t}\left(\frac{\partial L}{\partial \dot{\theta}_i}\right) - \frac{\partial L}{\partial \theta_i} \tag{8}$$

The ankle dynamics model is derived further.

$$T_1 = \left(J_1 + \frac{1}{4}m_1 d_1^2 + m_2 d_1^2\right)\ddot{\theta}_1 + \left(\frac{1}{2}m_1 + m_2\right) g d_1 \sin\theta_1 \tag{9}$$

The angular acceleration is expressed as $\ddot{\theta}_1$.

$$\ddot{\theta}_1 = \frac{1}{J}\left(T_1 - T_m\right) \tag{10}$$

where $J = J_1 + \frac{m_1 d_1^2 + 4 m_2 d_1^2}{4}$, $T_m = \left(\frac{m_1 + 2m_2}{2}\right) g d_1 \sin\theta_1$.

The ankle is driven by a driving wheel, and the driving torque is expressed as follows.

$$T_P = J_P \ddot{\theta}_1 \tag{11}$$

where J_P is the moment of inertia of the driving wheel. Considering the effects of damping and disturbance, the total driving torque is expressed as follows.

$$T = T_1 + T_P + \tau_d + c\dot{\theta}_1 \tag{12}$$

where τ_d is a disturbance, $c\dot{\theta}_1$ is the damping.

2.3. Static model of the PMA

Due to the complex structure of the PMA, its static characteristics are difficult to express with a theoretical model [30]. Therefore, the static model of the PMA is usually established based on theoretical research and experimental corrections. Fig. 3 shows the testing of the PMA, indicating that the contracting force is primarily affected by input gas pressure, initial length, and contracting length.

Within the range of input gas pressure from 0.1 MPa to 0.4 MPa and initial length from 165 mm to 200 mm, the following rules apply: when the input gas pressure is constant, the contracting force increases with the initial length. Conversely, for the same contracting force, a greater initial length requires a lower input gas pressure.

The characteristic model of the pneumatic muscle actuator is established as follows.

$$F(\varepsilon, p) = a(\varepsilon)\, p + b(\varepsilon) \tag{13}$$

where $a(\varepsilon) = \sum_{m=0}^{2} a_{2-m}\varepsilon^m$, $b(\varepsilon) = \sum_{n=0}^{4} b_{4-n}\varepsilon^n$.

By combining the theoretical model with experimental corrections, the parameter values in Eq. (13) are obtained using the fitting method, as shown in Table 1.

2.4. Analysis of output force

Fig. 4 shows the driving structure of the bionic robotic ankle, which imitates the human joint driving mechanism. The bionic ankle is equipped with pneumatic muscle actuators on both sides to mimic agonistic and antagonistic muscles. The ankle uses different combinations of PMAs to drive its movements.

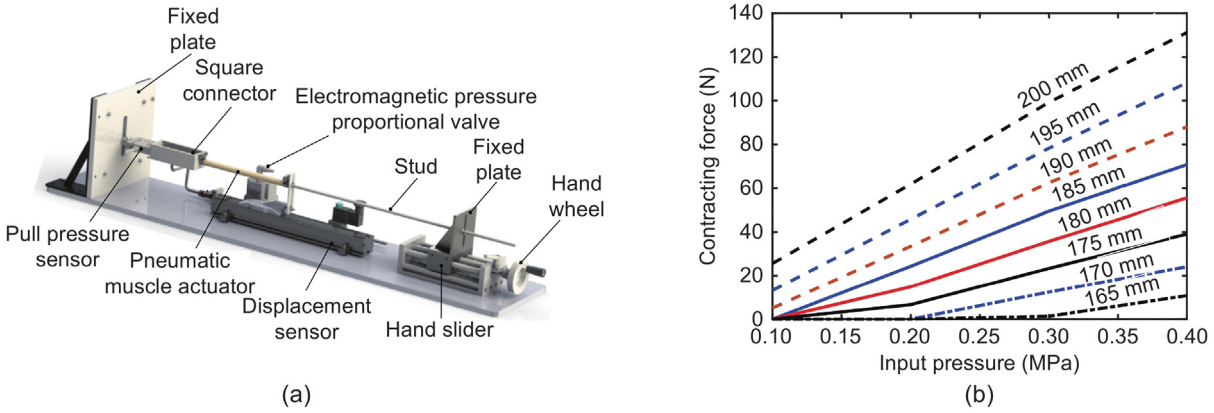

Fig. 3. The testing of the PMA. (a) The Testing device of the pneumatic muscle actuator. (b) The relationship between the contracting force and the input gas pressure.

Table 1
Multinomial curve fitting parameters.

Symbol	Value	Symbol	Value
a_0	−0.057	b_1	−0.00231
a_1	−7.247	b_2	0.132
a_2	355.3	b_3	−2.428
b_0	1.75×10^{-5}	b_4	−9.032

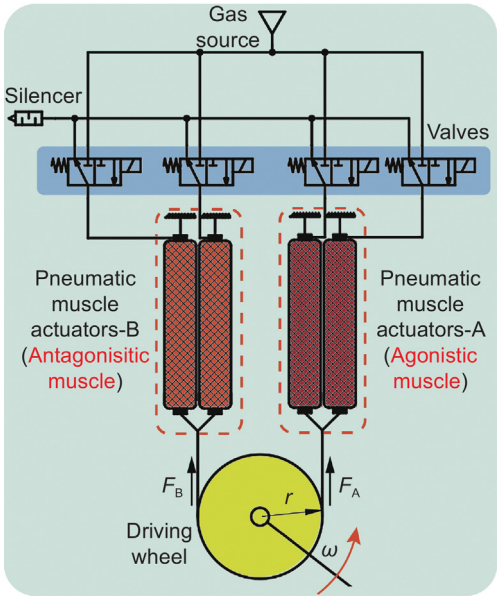

Fig. 4. Diagram of the multi-PMA bionic robotic ankle structure.

As shown in Fig. 4, when the bionic robotic ankle rotates counterclockwise, PMA-A is activated by the on–off valves, providing the driving force for rotation and acting as the agonistic muscle. Meanwhile, PMA-B is pulled, providing the antagonistic force and acting as the antagonistic muscle. Conversely, if the bionic ankle rotates clockwise, the roles of the agonistic and antagonistic muscles switch.

The output force is related to the number of the activated PMA. The control signal for the on–off valve connected to PMA-A is $x_A = x_i$, where $x_i = 1$ $(i = 1\sim4)$ indicates that the on–off valve is open and PMA-A is activated and contracting, while $x_i = 0$ $(i = 1\sim4)$ indicates that the on–off valve is closed, and PMA-A is exhausting. Similarly, the control signal for the on–off valves connected to PMA-B is $x_B = x_j$, where $x_j = 1$ $(i = 1\sim4)$ indicates that the on–off valve is open and PMA-B is activated and contracting, while $x_j = 0$ $(i = 1\sim4)$ indicates that the on–off valve is closed and PMA-B is exhausting. Thus, the relationship between the number of the activated PMA and the on–off valve signals can be represented.

$$n_A = \sum_{i=1}^{4} x_i \tag{14}$$

$$n_B = \sum_{j=1}^{4} x_j \tag{15}$$

According to Eqs. (13)–(15), the total output force of the bionic robotic ankle can be determined.

$$\begin{cases} F_A = F\left(\varepsilon_A, p_A\right) \cdot n_A \\ F_B = F\left(\varepsilon_B, p_B\right) \cdot n_B \end{cases} \tag{16}$$

$$\begin{cases} \varepsilon_A = \varepsilon_0 + r\theta_2 \\ \varepsilon_B = \varepsilon_0 - r\theta_2 \end{cases} \tag{17}$$

The equation for the output torque of the ankle is established.

$$\begin{aligned} T &= \left(F_A - F_B\right) r \\ &= \left(\sum_{i=1}^{4} x_i \cdot \left(a\left(\varepsilon_A\right) p_A + b\left(\varepsilon_A\right)\right) - \sum_{j=1}^{4} x_j \left(a\left(\varepsilon_B\right) p_B + b\left(\varepsilon_B\right)\right) \right) r \end{aligned} \tag{18}$$

The rate of change of torque is obtained by differentiating Eq. (18).

$$\begin{aligned} \dot{T} = \Bigg(& \sum_{i=1}^{4} x_i \left(a\left(\varepsilon_A\right) \dot{p}_A + \dot{a}\left(\varepsilon_A\right) p_A + \dot{b}\left(\varepsilon_A\right)\right) \\ & - \sum_{j=1}^{4} x_k \left(a\left(\varepsilon_B\right) \dot{p}_B + \dot{a}\left(\varepsilon_B\right) p_B + \dot{b}\left(\varepsilon_B\right)\right) \Bigg) r \end{aligned} \tag{19}$$

Eqs. (18) and (19) show that the output torque is affected by the number of the PMAs, the length of contraction, and the input gas pressure.

From Eqs. (18) and (19), it can be seen that different output torques can be achieved by adjusting the input gas pressure. Changes in the input gas pressure can be determined by differentiating the ideal gas equation [31,32].

$$\dot{p} = \frac{kRT}{V} q_m - \frac{kp\dot{V}}{V} \tag{20}$$

Where q_m is the mass flow rate, p is the gas pressure, V is the gas volume of the pneumatic muscle cavity, T is the adiabatic temperature of the gas, k is the adiabatic coefficient of gas, R is the gas constant.

Assuming that the PMA operates as an ideal cylinder, its volume V and volume change $\dot{V}$ can be obtained by using the geometric model.

$$\begin{cases} V = \frac{\pi D_0^2}{4\sin 2\alpha_0}(L_0-\varepsilon)\left(1-\frac{(L_0-\varepsilon)^2\cos 2\alpha_0}{L_0^2}\right) \\ \dot{V} = \frac{\pi D_0^2}{4\sin 2\alpha_0}\left(\frac{3(L_0-\varepsilon)^2\cos 2\alpha_0}{L_0^2}-1\right)\dot{\varepsilon} \end{cases} \tag{21}$$

where α_0 is the initial angle of the woven, D_0 is the initial diameter of the PMA, L_0 is the initial length of the PMA, ε is the length of contraction.

The on–off valve is controlled by pulse width modulation (PWM). Based on the gas mass flow equation [31,32], the relationship between gas flow and the duty cycle is established.

$$q_m = u\varphi_m(p_i, p_o) \tag{22}$$

$$\varphi_m(p_i, p_o) = \begin{cases} C_d S\frac{p_i}{\sqrt{RT}}\sqrt{\frac{2k}{k-1}\left[\left(\frac{p_o}{p_i}\right)^{\frac{2}{k}}-\left(\frac{p_o}{p_i}\right)^{\frac{k+1}{k}}\right]} & (p_{cr}\le\frac{p_o}{p_i}\le 1) \\ C_d S\frac{p_i}{\sqrt{RT}}\sqrt{\frac{2k}{k+1}\left(\frac{2}{k+1}\right)^{\left(\frac{2}{k-1}\right)}} & (\frac{p_o}{p_i}\le p_{cr}) \end{cases} \tag{23}$$

where, p_i is the upstream absolute pressure, p_o is the downstream absolute pressure. S is the equivalent cross-sectional area of the on–off valve.

When the contraction of the PMA is constant, the volume change is zero, and the rate of change of input gas pressure can be expressed.

$$\dot{p} = \frac{kRT}{V}q_m \tag{24}$$

It can be seen that the rate of change of input gas pressure is related to the internal mass flow rate.

When the contraction is fixed, the rate of change of output torque can be expressed.

$$\dot{T} = \frac{kRT}{V}\left(\sum_{i=1}^{4}x_i\cdot(u_A\varphi_{mA}a(\varepsilon_A)) - \sum_{j=1}^{4}x_j(u_B\varphi_{mB}a(\varepsilon_B))\right)r \tag{25}$$

It can be seen that when the combination of the on–off valves is fixed and the length of contraction is constant, the change in torque will also be affected by the PWM equivalent mass flow rate in one cycle. Therefore, controlling the duty cycle of the on–off valves can achieve different output torques.

3. Simulation of motion control

3.1. Force matching control strategy

Based on the human joint driving mechanism and the analysis of the bionic robotic ankle, the multi-PMA recruiting strategy is illustrated in Fig. 5.

First, determine the magnitude of the load F_l and the output force F_o. If $F_o < F_l$, it indicates that the output force from the current combination does not meet the load requirement, and it is necessary to increase the number of activated PMA, until $F_o \ge F_l$.

Second, compare the current angle error e with the limiting value δ. When $e \le |\delta|$, it indicates that the output force is optimal, and no adjustment is needed for n. When $e > \delta$, it indicates that the output force is insufficient, leading to an increase in error, which requires $n = n + 1$, Conversely, when $e < -\delta$, it means that the output force is too large, causing an increase in error, which requires $n = n - 1$.

Finally, $n \in [1, N]$. When $n \notin [1, N]$, if $n < 1$, $n = 1$; if $n > N$, $n = N$.

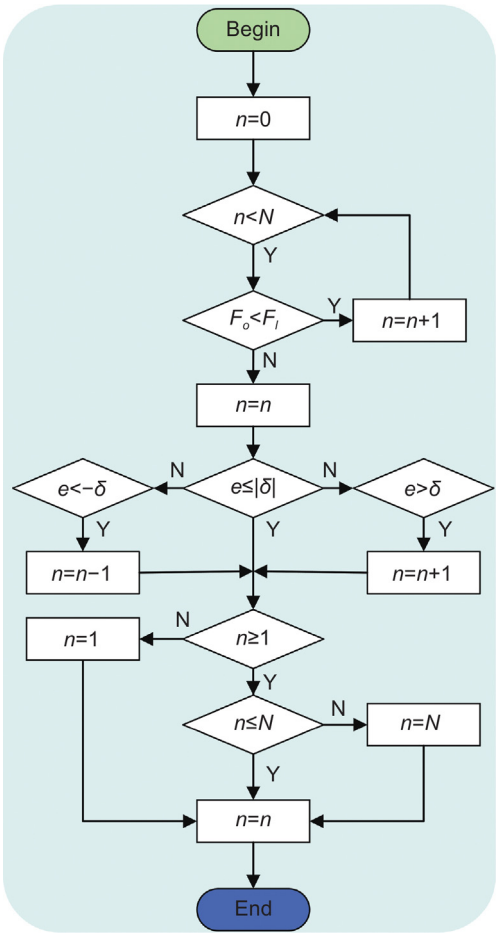

Fig. 5. Flow chart of the multi-PMA recruitment.

Fig. 6 shows the schematic diagram of the load matching control for the bionic robotic ankle. The pneumatic muscle actuators are arranged on both sides of the bionic robotic ankle, with motion driven and controlled by Pneumatic Muscle Actuators-A and Pneumatic Muscle Actuators-B. Both sides follow similar control principles. Within each control loop, a PID controller is used for feedback control of the rotation angle. The duty cycle of the PWM is calculated based on the difference between the expected angle and the feedback angle. The PWM generator controls the on–off valves, which activate the PMA and drive the ankle to rotate. In addition, the output force is regulated by a force matching controller using the multi-PMA recruitment strategy shown in Fig. 5, to further control the corresponding on–off valves and drive the ankle.

Simulated models are established in Simulink to conduct motion analysis for the ankle. The expected rotation is $\theta_d = 20\sin(t)$, the PWM frequency is 20 Hz, and the parameters of the PID controller are $K_p = 50$, $K_d = 5$, $K_i = 0$. Table 2 shows other simulation parameters.

3.2. Characteristics of output angle

Fig. 7 shows the characteristics of the output angle. From 0 to 1.6 s, the ankle undergoes sagittal dorsiflexion, with the first peak

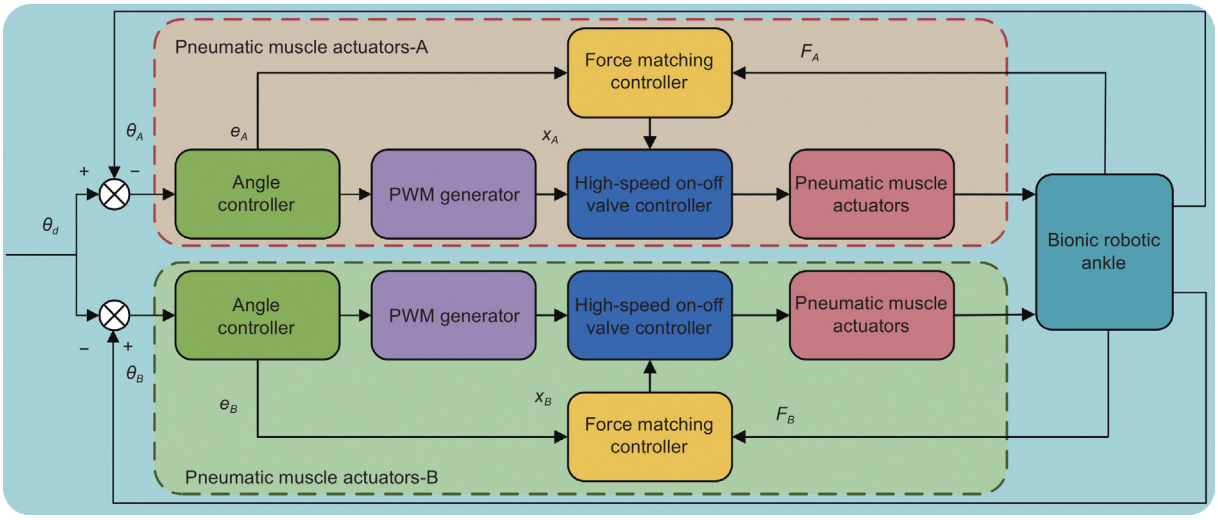

Fig. 6. Schematic diagram of bionic robotic ankle load matching control.

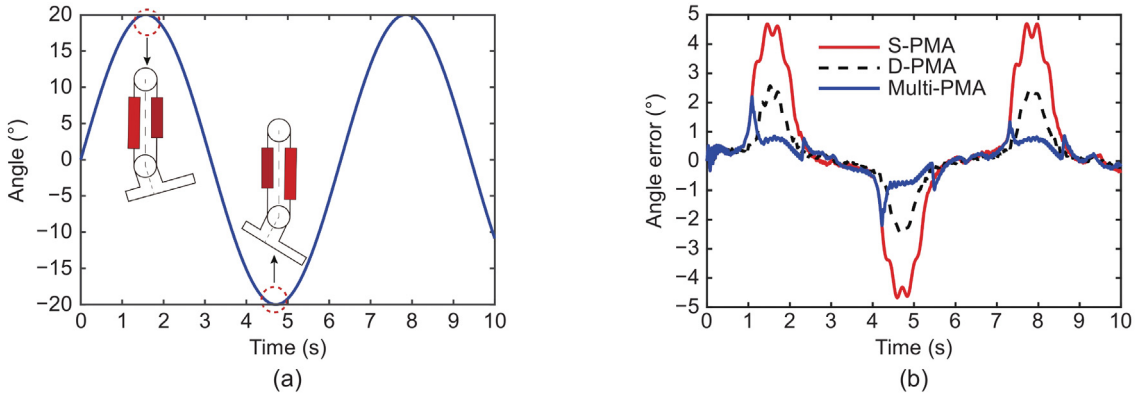

Fig. 7. The characteristics of output angle. (a) The expected output angle curve of the ankle. (b) Output angle error of the different driving types.

Table 2
Parameters in the simulation.

Name	Symbol	Value
source gas pressure	Ps	0.4 MPa
Diameter of the PMA	D_0	12.5 mm
Initial length of the PMA	L_0	200 mm
Diameter of the valve port	D	1 mm
Quality of the driving wheel	m_p	0.2 kg

representing the maximum dorsiflexion angle and the maximum contraction length of the agonistic muscle. From 1.6 to 4.7 s, the ankle performs plantarflexion, with the first trough indicating the largest plantarflexion angle and the maximum contraction of the antagonistic muscle. After 4.7 s, the ankle rotates again into dorsiflexion, repeating the previous movement.

To study the motion characteristics of the Multi-PMA bionic robotic ankle, the bilateral single pneumatic muscle actuator robotic ankle (S-PMA robotic ankle) and bilateral dual pneumatic actuator robotic ankle (D-PMA robotic ankle) are selected for comparative analysis.

Fig. 7(b) shows the angle errors for the three types of ankles (with a load mass of 3 kg). It is evident that the output angle error of the S-PMA robotic ankle is the largest, the output angle error of the D-PMA robotic ankle is larger, and the output angle error of the Multi-PMA bionic robotic ankle is the smallest. This demonstrates the precision advantage of the bionic Multi-PMA mechanism in driving joint.

3.3. Characteristics of output force

Fig. 8 shows the output force curve of the S-PMA robotic ankle. In Fig. 8(a), the solid blue line represents the load, the dotted red line represents the output force of the S-MPA-A, and the solid black line represents the theoretical maximum output force of the S-PMA-A.

From 0 to 1.1 s, as the dorsiflexion angle increases, the contraction length of the S-PMA-A which acts as the agonistic muscle also increases, causing its theoretical output force to decrease. At 1.1 s, the maximum output force of the S-PMA-A is less than the load, making it insufficient to drive ankle dorsiflexion. It is not until 2.2 s that the ankle transitions into plantarflexion rotation, with the S-PMA-B working as the agonistic muscle, as shown by the red dotted line in Fig. 8(b). At 4.2 s, the maximum output force of the S-PMA-B is less than the load, making it insufficient to drive ankle plantarflexion. At 5.4 s, the ankle transitions back into dorsiflexion, and the S-PMA-A again acts as the agonistic muscle, continuing to drive the ankle's rotation. The curve in Fig. 8 shows that the S-PMA has phases of insufficient output force, resulting in halted motion and failing to rotate according to the expected curve.

To achieve ankle rotation according to the desired trajectory, the traditional method is to increase the number of pneumatic muscle actuators. This paper simulates the driving mode with dual pneumatic muscle actuators on both sides. The output characteristic curve is shown in Fig. 9. The driving characteristics of

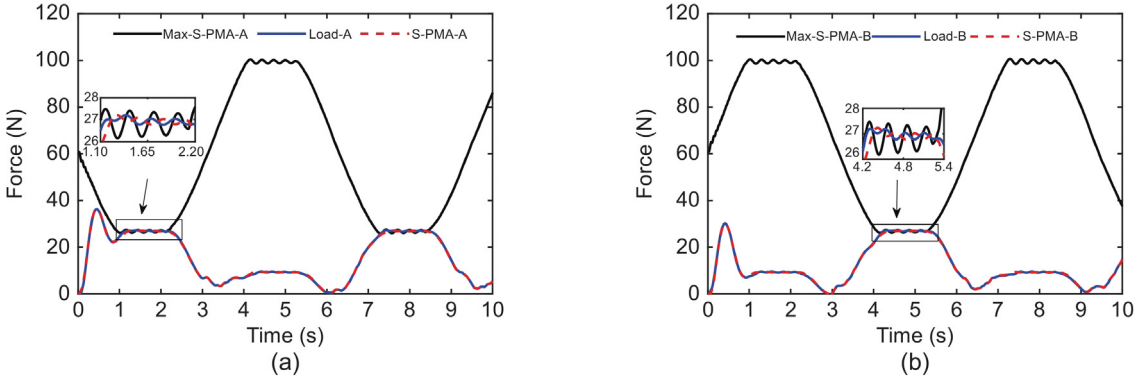

Fig. 8. Output force curves of the S-PMA robotic ankle. (a) Output force curve of the S-PMA-A. (b) Output force curve of the S-PMA-B.

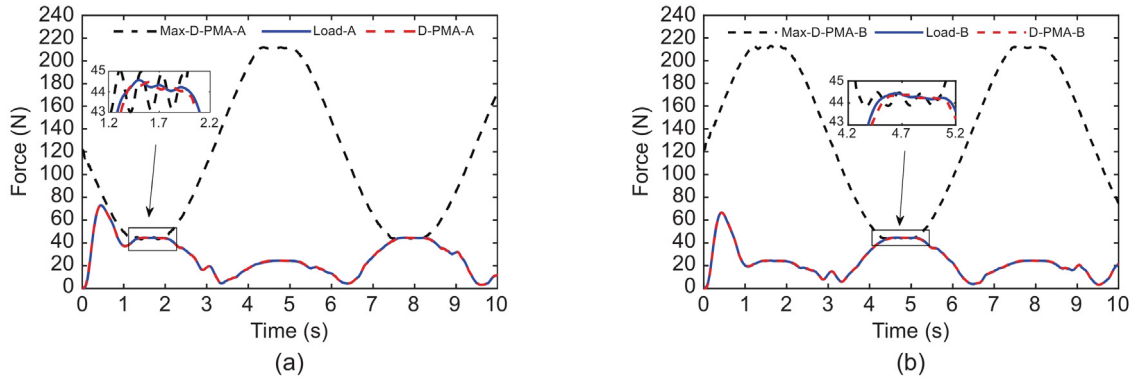

Fig. 9. Output force curves of the D-PMA robotic ankle. (a) Output force curve of the D-PMA-A. (b) Output force curve of the D-PMA-B.

the D-PMA are similar to those of the S-PMA. When the agonistic muscle provides power to the ankle, it is pulled by the antagonistic muscle. Near the maximum angles in dorsiflexion and plantarflexion, the output torque cannot meet the load, resulting in motion stagnation. In the motion of the D-PMA robotic ankle, the stagnation time are from 1.2 to 2.0 s and from 4.3 to 5.2 s.

To address the aforementioned shortcomings, this paper proposes a bionic driving mechanism based on the multi-muscle recruitment mechanism of the human joint. Fig. 10 shows the driving characteristics of the multi-PMA. In Fig. 10(a), the solid blue line represents the load, the dotted red line represents the output force of the Multi-PMA-A, and the solid black line represents the theoretical maximum output force of the Multi-PMA-A. Clearly, the black dotted line is always above the blue solid line, indicating that the output force of the multi-PMA can drive the load. From 0 to 1.0 s, as the dorsiflexion angle increases, the contraction length of the Multi-PMA-A, which acts as the agonistic muscle, also increases, and its theoretical output force decreases but remains greater than the load, allowing the ankle to rotate. During this period, the Multi-PMA bionic robotic ankle recruits a single pneumatic actuator. From 1.0 to 2.4 s, the output force of a single pneumatic muscle is insufficient to drive the ankle to rotate, so the Multi-PMA recruits two pneumatic muscle actuators. On the side of the antagonistic muscle, the driving force required only necessitates the recruitment of a single pneumatic muscle, as shown in Fig. 10(b). The black dotted line is always above the blue solid line, indicating that the antagonistic muscle does not need to recruit additional pneumatic muscle actuators.

By comparing the driving characteristics of the S-PMA robotic ankle, the D-PMA robotic ankle, and the Multi-PMA bionic robotic ankle, we can see that the first two driving strategies use an all-or-nothing selection model. In contrast, the bionic strategy can output different forces to drive various loads by adjusting the number of recruited pneumatic muscle actuators.

4. Experiment and discussion

As shown in Fig. 11, an experimental testing platform is built to analyze the driving characteristics of the ankles. The solid black line represents the flow of pressurized gas, and the dashed black line represents the flow of electronic signals. The experimental components include an air compressor, MCU (STM32F103C8T6), on–off valve (H103L-DL), rotary encoder (GTH08-LD-RAG2500Z1-2M), and force transducer. The air compressor provides pressurized gas, which is controlled by the on–off valve and delivered to the PMA. The microcomputer processes the angle information and the output force information in real-time, which is used to track the position and activate the on–off valve to achieve load matching control.

The black dotted line indicates the direction of electrical signal transmission, and the black solid line indicates the flow direction of fluid energy. The air pump converts mechanical energy into fluid energy transfer. The compressed gas first passes through the pneumatic triplet (mainly used to set the safety test pressure), then through the pipeline to the on–off valve (mainly used to control the intake and output volume of the pneumatic muscle), and finally, the gas is transferred to the pneumatic muscle. Pneumatic muscles convert fluid energy into mechanical energy to drive the bionic ankle movement. The slave computer collects force sensor data, angle encoder data, and performs closed-loop control of the bionic ankle joint. The slave computer adjusts PWM through the position controller program according to the angle encoder information and controls the on–off valve through corresponding pulse width modulation, based on its duty cycle, to manage the intake and exhaust volume of the pneumatic muscle. The force sensor information helps determine the numbers of pneumatic muscles involved in the movement through the force matching controller program. The PC collects and processes data from the

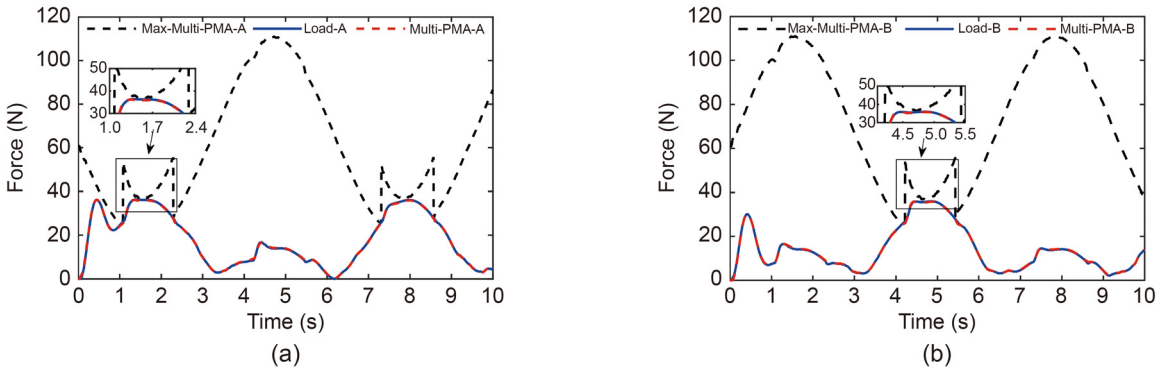

Fig. 10. Output force curves of the Multi-PMA-A robotic ankle. (a) Output force curve of the Multi-PMA-A. (b) Output force curve of the Multi-PMA-B.

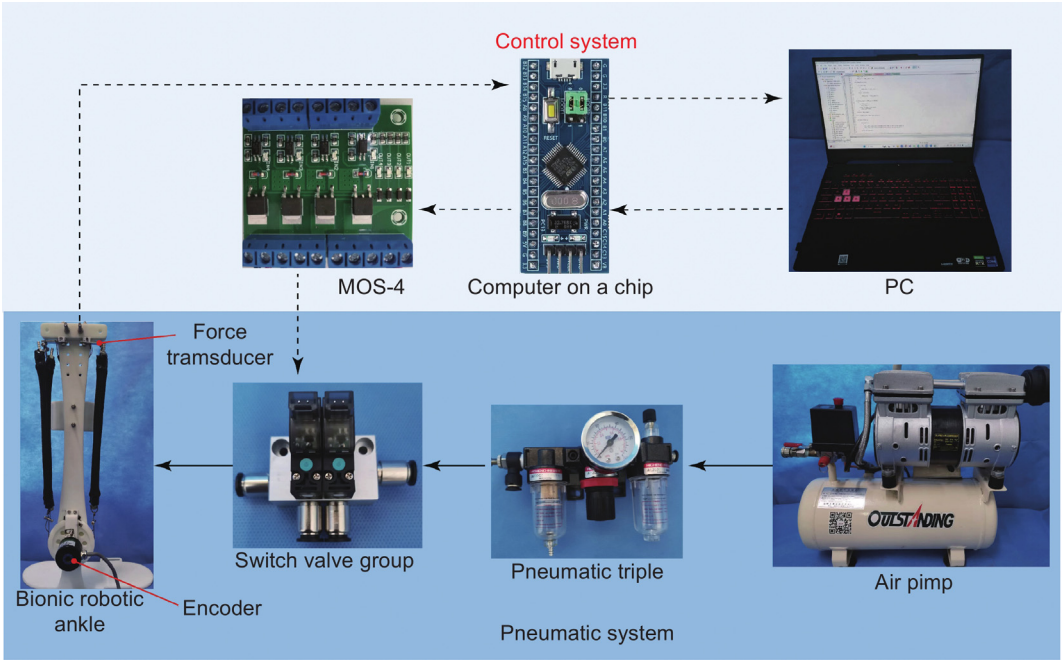

Fig. 11. Schematic diagram of the ankle experimental system.

slave computer and delivers the movement pattern of the bionic ankle joint.

Set the air source pressure to 0.4 MPa and configure the desired angle curves to $\theta_d = 20\sin(t)$ and $\theta_d = 20\sin(2t)$, respectively. The parameters of the PID controller are $K_p = 1000$, $K_d = 50$, $K_i = 0$.

The output characteristic curves of the bionic Multi-PMA robotic ankle, with the desired angle set to $\theta_d = 20\sin(t)$, and a unilateral PMA count of 2, are shown in Fig. 12. As seen in Fig. 12(a), the maximum angle of plantarflexion and dorsiflexion is about 16°. Referring to Fig. 12(b), when the plantarflexion angle is 16°, Multi-PMA-A acts as the agonistic muscle and recruits 2 PMAs, while Multi-PMA-B acts as the antagonistic muscle and recruits 1 PMA. Conversely, when the dorsiflexion angle is 16°, Multi-PMA-B acts as the agonistic muscle and recruits 2 PMAs, while Multi-PMA-A acts as the antagonist muscle and recruits 1 PMA. The limitation on the number of PMAs resulted in a significant deviation of the maximum angle of plantarflexion and dorsiflexion from the desired angle.

The output characteristic curves of the bionic Multi-PMA robotic ankle, with the desired angle set to $\theta_d = 20\sin(t)$ and the unilateral PMA count set to 4, are shown in Fig. 13. As can be seen from Fig. 13(a), the actual angle tracks the desired angle well. Referring to Fig. 13(b), when the plantarflexion angle increases from 0 to 20° over 0–5 s, the number of PMAs recruited by Multi-PMA-A as the agonistic muscle increases from 0 to 4, while the number of PMAs recruited by Multi-PMA-B as the antagonistic muscle increases from 0 to 2. At a dorsiflexion angle of 20°, Multi-PMA-B acts as the agonistic muscle, and the number of PMAs recruited is 3. Due to the increase in the number of PMAs and the variety of combinations of recruited PMAs, the angle can accurately track the desired angle.

The output characteristic curves of the bionic Multi-PMA robotic ankle are shown in Fig. 14 when the desired angle is $\theta_d = 20\sin(2t)$ and the number of unilateral PMAs is 4. The bionic Multi-PMA robotic ankle is also able to track the desired angle by doubling the angle frequency of $\theta_d = 20\sin(2t)$ compared to $\theta_d = 20\sin(t)$. Corresponding to Fig. 14(b), the frequency of PMA recruitment is more intensive compared to Fig. 13(b).

The error curves of the bionic Multi-PMA robotic ankle for desired angles $\theta_d = 20\sin(t)$ and $\theta_d = 20\sin(2t)$ are shown in Fig. 15. As seen in Fig. 15(a), when the desired angle is $\theta_d = 20\sin(t)$, the error curve for 2 PMAs ranges from $[-3.7, 3.4]$, while the error curve for 4 PMAs ranges from $[-3.3, 2.2]$. Overall, the error curve for 4 PMAs is better than that for 2 PMAs. When the desired angle frequency is doubled to $\theta_d = 20\sin(2t)$, the

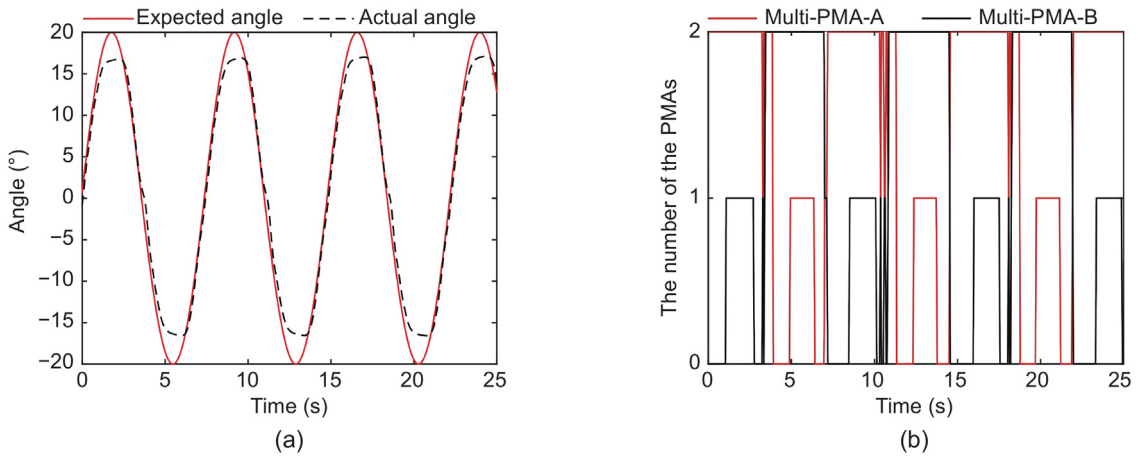

Fig. 12. Output characteristic curve of the Multi-PMA bionic robotic ankle with 2 PMAs. (a) Motion angle curve. (b) PMA recruitment curve.

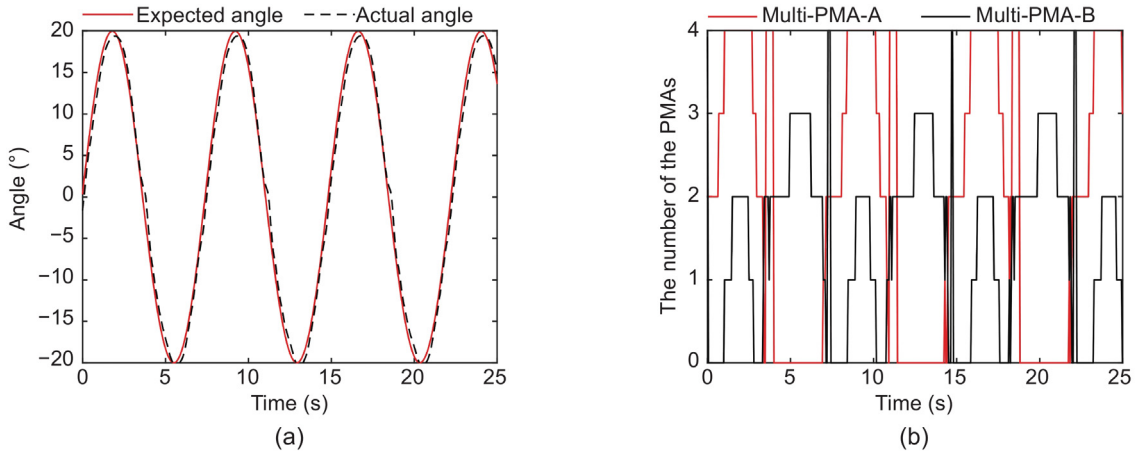

Fig. 13. Output characteristic curve of the Multi-PMA bionic robotic ankle with 4 PMAs. (a) Motion angle curve. (b) PMA recruitment curve.

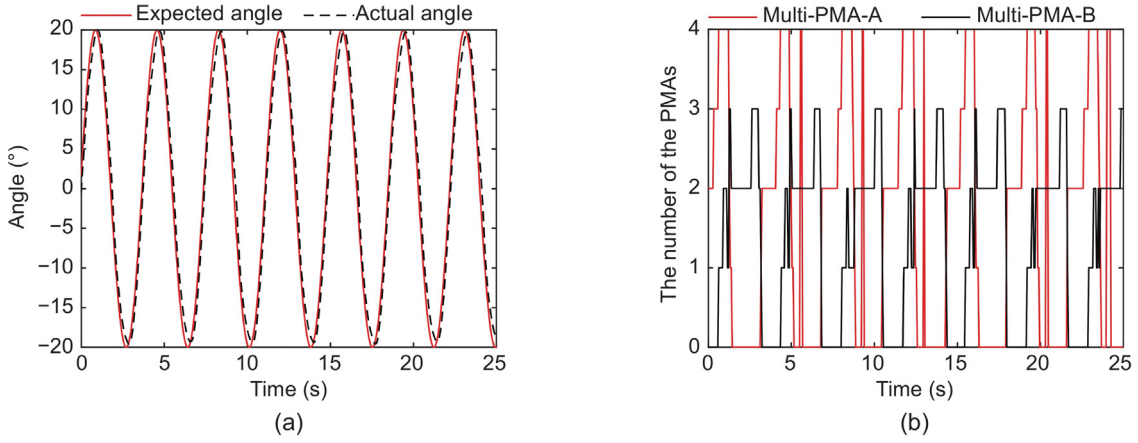

Fig. 14. Output characteristic curve of the Multi-PMA bionic robotic ankle with 4 PMAs. (a) Motion angle curve. (b) PMA recruitment curve.

error curves of the PMAs are shown in Fig. 15(b). The error curve for 2 PMAs ranges from [−5, 4.3], and the error curve for 4 PMAs ranges from [−4.3, 3]. The error curve for 4 PMAs is smaller than that for 2 PMAs. As the expected angle frequency increases, the error of the PMAs also increases, which is attributed to multiple factors such as the delayed response of the on–off valve and the jittering of the PMAs.

The root mean square errors (RMSEs) of the angle for the bionic Multi-PMA robotic ankle are shown in Table 3. When the desired angle frequency is 1 Hz, that is, the desired angle is $\theta_d = 20\sin(t)$, the RMSE of the angle for 2 PMAs is 2.0056, while the RMSE for 4 PMAs is 1.2602. The RMSE for 4 PMAs is smaller than that for 2 PMAs. When the desired angle frequency is 2 Hz, that is, the desired angle is $\theta_d = 20\sin(2t)$, the RMSE

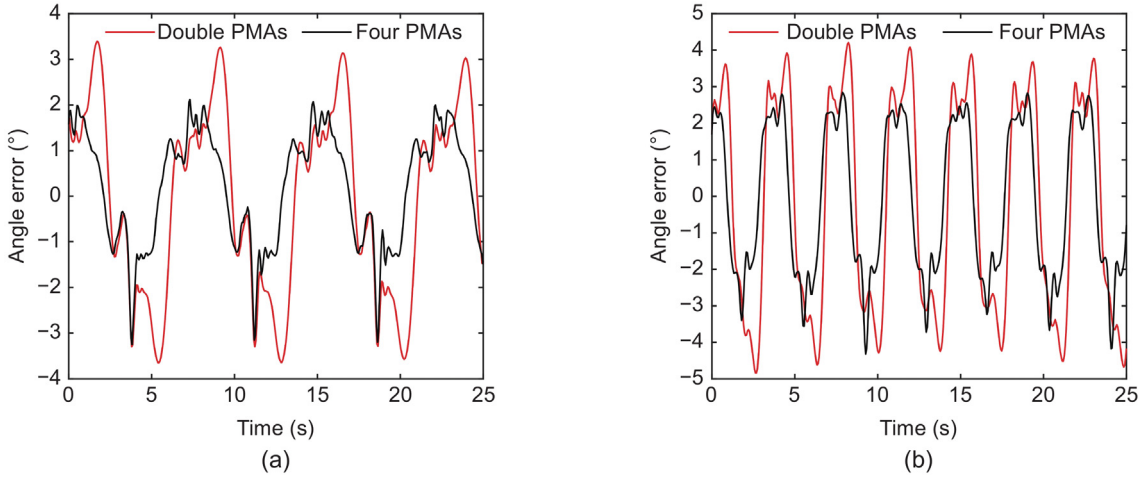

Fig. 15. Angle error curves of the bionic Multi-PMA robotic ankle at different frequencies. (a) $y = 20\sin(t)$, (b) $y = 20\sin(2t)$.

Table 3
The root mean square errors of the angle of the bionic Multi-PMA robotic ankle.

Model	$y = 20\sin(t)$	$y = 20\sin(2t)$
Double PMAs	2.0056	2.9861
Four PMAs	1.2602	2.1005

of the angle for 2 PMAs is 2.9861, and the RMSE for 4 PMAs is 2.1005. The RMSEs for both 2 PMAs and the 4 PMAs increase compared to the 1 Hz frequency, which is due to the response rate of the on–off valve and the hysteresis of the PMAs. When dealing with heavy loads, increasing the number of the PMAs recruited by the bionic Multi-PMA robotic ankle helps to reduce angle errors and improve tracking accuracy. However, increasing the frequency can cause an increase in angle errors.

5. Conclusion

In this paper, a novel bionic robotic ankle driven by multiple pneumatic muscle actuators is studied. The bionic design, theoretical analysis, simulation analysis and experimental testing are completed. The following conclusions are obtained.

The bionic structure and driving mechanism are designed by imitating the multi-motor unit and recruitment mechanism of human skeletal muscle. Different combinations of 4 pneumatic muscle actuators on one side can drive a wide range of loads. The driving characteristics of the bionic ankle are studied theoretically, dynamic and the PMA models are established to show how output torque, the number of PMAs, the contraction length, and input gas pressure influence performance. Based on the Multi-PMA recruitment strategy, load-matching control simulations for agonistic and antagonistic muscles are carried out, and the output characteristics of the S-PMA robotic ankle, the D-PMA robotic ankle, and the Multi-PMA bionic robotic ankle are obtained. Finally, a prototype of the bionic ankle is developed, and the motion control testing is completed. This testing proves that the Multi-PMA bionic robotic ankle can drive the joint in real-time according to load changes, indicating superior angle tracking performance compared to other PMA robotic ankles.

CRediT authorship contribution statement

Delei Fang: Writing – original draft, Validation, Supervision, Project administration, Conceptualization. **Fangyuan Ren:** Validation, Formal analysis. **Jianwei Wang:** Software, Investigation. **Pan Li:** Validation, Investigation. **Lin Cao:** Conceptualization. **Junxia Zhang:** Validation, Resources, Conceptualization.

Declaration of competing interest

The authors declare that they have no known competing financial interests or personal relationships that could have appeared to influence the work reported in this paper.

Acknowledgments

This work was partly supported by the National Natural Science Foundation of China (52005369), Open Project Fund of Tianjin Key Laboratory of Integrated Design and Online Monitoring of Light Industry and Food Engineering Machinery and Equipment (2020LIMFE05).

Appendix A. Supplementary data

Supplementary material related to this article can be found online at https://doi.org/10.1016/j.birob.2024.100176.

References

[1] C. Yang, Y. Jiang, W. He, J. Na, Z. Li, B. Xu, Adaptive parameter estimation and control design for robot manipulators with finite-time convergence, IEEE Trans. Ind. Electron. 65 (10) (2018) 8112–8123.
[2] M. Hamaya, T. Matsubara, T. Teramae, T. Noda, J. Morimoto, Design of physical user–robot interactions for model identification of soft actuators on exoskeleton robots, Int. J. Robot. Res. 40 (1) (2021) 397–410.
[3] L. Zhao, H. Cheng, J. Zhang, Y. Xia, Adaptive control for a motion mechanism with pneumatic artificial muscles subject to dead-zones, Mech. Syst. Signal Process. 148 (2021) 107155.
[4] C. Fu, K. Wang, W. Tang, A. Nilghaz, C. Hurren, X. Wang, Z. Xia, Multi-sensorized pneumatic artificial muscle yarns, Chem. Eng. J. 446 (2022) 137241.
[5] Y. Yuan, Y. Yu, L. Guo, Nonlinear active disturbance rejection control for the pneumatic muscle actuators with discrete-time measurements, IEEE Trans. Ind. Electron. 66 (3) (2019) 2044–2053.
[6] N. Sun, D. Liang, Y. Wu, Y. Chen, Y. Qin, Y. Fang, Adaptive control for pneumatic artificial muscle systems with parametric uncertainties and unidirectional input constraints, IEEE Trans. Ind. Inform. 16 (2) (2020) 969–979.
[7] L.A. Tuan, Neural observer and adaptive fractional-order backstepping fast-terminal sliding-mode control of RTG cranes, IEEE Trans. Ind. Electron. 68 (1) (2021) 434–442.
[8] J. Huang, Y. Cao, C. Xiong, H.-T. Zhang, An echo state gaussian process-based nonlinear model predictive control for pneumatic muscle actuators, IEEE Trans. Autom. Sci. Eng. 16 (3) (2019) 1071–1084.
[9] J. Zhong, J. Fan, J. Zhao, W. Zhang, Kinematic analysis of jumping leg driven by artificial muscles, in: The Proceedings of IEEE International Conference on Mechatronics and Automation, ICMA, Chengdu, China, 2012, pp. 1004–1008.

[10] T.-C. Tsai, M.-H. Chiang, A lower limb rehabilitation assistance training robot system driven by an innovative pneumatic artificial muscle system, Soft Robotics 10 (1) (2023) 1–16.
[11] T.-C. Tsai, M.-H. Chiang, Design and control of a 1-DOF robotic lower-limb system driven by novel single pneumatic artificial muscle, Appl. Sci. 10 (1) (2019) 43.
[12] B. Jamil, H. Rodrigue, Y. Choi, Design of a novel sensing method for a pneumatic artificial muscle actuator-driven 2-degrees of freedom parallel joint, Soft Robotics 10 (1) (2023) 187–196.
[13] H. Iijima, K. Sayama, H. Masuta, A. Takanishi, H. Lim, Mechanism of one-legged jumping robot with artificial musculoskeletal system, in: The Proceedings of International Conference on Control, Automation and Systems, (ICCAS), Gwangju, Korea (South), 2013, pp. 869–874.
[14] D. Liang, N. Sun, Y. Wu, Y. Chen, Y. Fang, L. Liu, Energy-based motion control for pneumatic artificial muscle actuated robots with experiments, IEEE Trans. Ind. Electron. 69 (7) (2022) 7295–7306.
[15] Y. Zhao, K. Qian, S. Bo, Z. Zhang, Z. Li, G.-Q. Li, et al., Adaptive co-operative control strategy for a wrist exoskeleton using model-based joint impedance estimation, IEEE/ASME Trans. Mechatronics 28 (2) (2023) 748–757.
[16] W.L. Chu, C.J. Lin, Y.Y. Chen, Redundant robot with pneumatic artificial muscles for rehabilitation works using iterative learning control, Appl. Sci. 12 (17) (2022) 8419.
[17] D. Xie, Y. Su, X. Shi, et al., A compact elbow exosuit driven by pneumatic artificial muscles, IEEE Robot. Autom. Lett. 9 (4) (2024) 3331–3338.
[18] M.U.A. Khan, A. Ali, R. Muneer, et al., Pneumatic artificial muscle-based stroke rehabilitation device for upper and lower limbs, Intelligent Service Robotics 17 (1) (2024) 33–42.
[19] Y. Wang, Q. Xu, Design and testing of a soft parallel robot based on pneumatic artificial muscles for wrist rehabilitation, Sci. Rep. 11 (1) (2021) 1273.
[20] H.T. Nguyen, V.C. Trinh, T.D. Le, An adaptive fast terminal sliding mode controller of exercise-assisted robotic arm for elbow joint rehabilitation featuring pneumatic artificial muscle actuator[c]//actuators, MDPI 9 (4) (2020) 118.
[21] C.T. Chen, W.Y. Lien, C.T. Chen, et al., Dynamic modeling and motion control of a cable-driven robotic exoskeleton with pneumatic artificial muscle actuators, IEEE Access 8 (2020) 149796–149807.
[22] H. Chi, H. Su, W. Liang, et al., Control of a rehabilitation robotic device driven by antagonistic soft actuators[c]//actuators, MDPI 10 (6) (2021) 123.
[23] T.C. Tsai, M.H. Chiang, Design and control of a 1-DOF robotic lower-limb system driven by novel single pneumatic artificial muscle, Appl. Sci. 10 (1) (2019) 43.
[24] H.R. Chu, S.J. Chiou, I.H. Li, et al., Design, development, and control of a novel upper-limb power-assist exoskeleton system driven by pneumatic muscle actuators[c]//actuators, MDPI 11 (8) (2022) 231.
[25] Q. Liu, Y. Liu, Y. Li, et al., Path planning and impedance control of a soft modular exoskeleton for coordinated upper limb rehabilitation, Front. Neurorobotics 15 (2021) 745531.
[26] H.P. Huy Anh, N.N. Son, C. Van Kien, Adaptive neural compliant force-position control of serial PAM robot, J. Intell. Robot. Syst. 89 (3–4) (2018) 351–369.
[27] M. Mara, J.P. Stein, M.E. Latoschik, et al., User responses to a humanoid robot observed in real life, virtual reality, 3D and 2D, Frontiers in psychology 12 (2021) 633178.
[28] T. Hoang, A. Kharchenko, S. Trendel, et al., Ball-and-Socket Joint Pose Estimation using Magnetic Field[C]//the International Symposium of Robotics Research, Springer Nature Switzerland, Cham, 2022, pp. 321–334.
[29] H. Yang, G. Wei, L. Ren, Development and characteristics of a highly biomimetic robotic shoulder inspired by musculoskeletal mechanical intelligence, IEEE Trans. Robot. (2024).
[30] A. Pujana-Arrese, A. Mendizabal, J. Arenas, R. Prestamero, J. Landaluze, Modelling in modelica and position control of a 1-DOF set-up powered by pneumatic muscles, Mechatronics 20 (5) (2010) 535–552.
[31] B. Jamil, S. Lee, Y. Choi, Conductive knit-covered pneumatic artificial muscle (k-PAM) actuator, in: The Proceedings of IEEE/RSJ International Conference on Intelligent Robots and Systems, (IROS), Madrid, Spain, 2018, pp. 1476–1481.
[32] B. Jamil, Y. Choi, Modified stiffness-based soft optical waveguide integrated pneumatic artificial muscle (PAM) actuators for contraction and force sensing, IEEE/ASME Trans. Mechatronics 26 (6) (2021) 3243–3253.